

Measurement of reactor antineutrino oscillation at SNO+

M. Abreu,^{1,2} V. Albanese,^{3,4} A. Allega,³ R. Alves,⁵ M. R. Anderson,³ S. Andringa,¹ L. Anselmo,⁶ J. Antunes,^{1,2}
 E. Arushanova,⁷ S. Asahi,³ M. Askins,^{8,9,10} D. M. Asner,^{6,11} D. J. Auty,¹² A. R. Back,^{7,13} S. Back,^{6,3}
 A. Bacon,¹⁴ T. Baltazar,^{1,2} F. Barão,^{1,2} Z. Barnard,⁴ A. Barr,⁶ N. Barros,^{15,16,14,17,1} D. Bartlett,³ R. Bayes,^{3,4}
 C. Beaudoin,^{4,3} E. W. Beier,¹⁴ G. Berardi,^{6,3} T. S. Bezerra,¹³ A. Bialek,^{6,4,3,12} S. D. Biller,¹⁸ E. Blucher,¹⁹
 A. Boeltzig,¹⁷ R. Bonventre,^{8,9,14} M. Boulay,³ D. Braid,⁴ E. Caden,^{6,4,3} E. J. Callaghan,^{8,9,14} J. Caravaca,^{8,9}
 J. Carvalho,^{5,16} L. Cavalli,¹⁸ D. Chauhan,^{6,3,1,4} M. Chen,³ S. Cheng,³ O. Chkvorets,⁴ K. J. Clark,^{3,13,18}
 B. Cleveland,^{6,4} C. Connors,⁴ D. Cookman,^{20,18} J. Corning,³ I. T. Coulter,^{14,18} M. A. Cox,^{21,1} D. Cressy,⁴
 X. Dai,³ C. Darrach,⁴ S. DeGraw,¹⁸ R. Dehghani,³ J. Deloye,⁴ M. M. Depatie,^{3,4} F. Descamps,^{8,9} C. Dima,¹³
 J. Dittmer,¹⁷ K. H. Dixon,²⁰ F. Di Lodovico,^{20,7} A. Doxtator,⁶ N. Duhaime,⁴ F. Duncan,^{6,4} J. Dunger,^{7,18}
 A. D. Earle,¹³ M. S. Esmaeilian,¹² D. Fabris,^{6,3} E. Falk,¹³ A. Farrugia,⁴ N. Fatemighomi,^{6,3} C. Felber,⁴ V. Fischer,¹⁰
 E. Fletcher,³ R. Ford,^{6,4} K. Frankiewicz,²² N. Gagnon,⁶ A. Gaur,¹² J. Gauthier,^{3,6} A. Gibson-Foster,¹³ K. Gilje,¹²
 O. I. González-Reina,²³ D. Gooding,²² P. Gorel,¹² K. Graham,³ C. Grant,^{22,10} J. Grove,^{3,4} S. Grullon,¹⁴ E. Guillian,³
 R. L. Hahn,¹¹ S. Hall,⁶ A. L. Hallin,¹² D. Hallman,⁴ S. Hans,¹¹ J. Hartnell,¹³ P. Harvey,³ C. Hearn,³ M. R. Hebert,^{8,9}
 M. Hedayatipour,¹² W. J. Heintzelman,¹⁴ J. Heise,³ R. L. Helmer,²⁴ C. Hewitt,¹⁸ B. Hodak,³ M. Hodak,^{6,3}
 M. Hood,⁶ D. Horne,³ M. Howe,²⁵ B. Hreljac,^{3,4} J. Hu,¹² P. Huang,¹⁸ R. Hunt-Stokes,¹⁸ T. Iida,³ A. S. Inácio,^{18,1,26}
 C. M. Jackson,^{8,9} N. A. Jelley,¹⁸ C. J. Jillings,^{6,4} C. Jones,¹⁸ P. G. Jones,^{7,18} S. Kaluzienski,³ K. Kamdin,^{8,9}
 T. Kaptanoglu,^{8,9,14} J. Kaspar,²⁷ K. Keeter,²⁸ C. Kefelian,^{8,9} P. Khaghani,⁴ L. Kippenbrock,²⁷ J. Kladnik,¹
 J. R. Klein,¹⁴ R. Knapik,^{14,29} J. Kofron,²⁷ L. L. Kormos,³⁰ S. Korte,⁴ B. Krar,³ C. Kraus,^{6,3} C. B. Krauss,¹²
 T. Kroupová,^{14,18} K. Labe,¹⁹ F. Lafleur,⁶ C. Lake,⁴ I. Lam,³ C. Lan,³ B. J. Land,^{14,8,9} R. Lane,⁷ S. Langrock,⁷
 P. Laroche,^{6,3} S. Larose,⁶ A. LaTorre,¹⁹ I. Lawson,^{6,4} L. Lebanowski,^{8,9,14} J. Lee,³ C. Lefebvre,³ G. M. Lefevre,¹³
 E. J. Leming,^{13,18} A. Li,²² O. Li,⁶ J. Lidgard,¹⁸ B. Liggins,⁷ P. Liimatainen,⁶ Y. H. Lin,^{3,4,6} X. Liu,³ Y. Liu,³
 V. Lozza,^{1,26,17} M. Luo,¹⁴ S. Maguire,^{6,11,4} A. Maio,^{1,26} K. Majumdar,¹⁸ S. Manecki,^{6,3} J. Maneira,^{1,26}
 R. D. Martin,³ E. Marzec,¹⁴ A. Mastbaum,^{19,14} A. Mathewson,⁶ N. McCauley,²¹ A. B. McDonald,³ K. McFarlane,⁶
 P. Mekarski,¹² M. Meyer,¹⁷ C. Miller,³ C. Mills,¹³ G. Milton,¹⁸ M. Mlejnek,¹³ E. Mony,³ B. Morissette,⁶ D. Morris,³
 I. Morton-Blake,¹⁸ M. J. Mottram,^{13,7} M. Mubasher,¹² S. Nae,^{1,26} S. Naugle,¹⁴ M. Newcomer,¹⁴ M. Nirkko,¹³
 L. J. Nolan,^{4,7} V. M. Novikov,³ H. M. O'Keeffe,^{30,3} E. O'Sullivan,³ G. D. Orebi Gann,^{8,9,14} S. Ouyang,^{31,32}
 J. Page,^{3,13} S. Pal,³ K. Paleshi,⁴ W. Parker,¹⁸ M. J. Parnell,³⁰ J. Paton,¹⁸ S. J. M. Peeters,¹³ T. Pershing,¹⁰
 Z. Petriw,¹² J. Petzoldt,¹⁷ L. J. Pickard,^{8,9,10} D. Pracovics,⁴ G. Prior,¹ J. C. Prouty,^{8,9} B. Quenallata,^{15,16}
 S. Quirk,³ P. Ravi,⁴ S. Read,⁶ A. Reichold,¹⁸ M. Reinhard,¹⁷ S. Riccetto,³ M. Rigan,¹³ I. Ritchie,⁶ A. Robertson,²¹
 B. C. Robertson,³ J. Rose,²¹ R. Rosero,¹¹ P. M. Rost,⁴ J. Rumleskie,⁴ A. Sörensen,¹⁷ P. Schrock,¹⁷ M. A. Schumaker,⁴
 M. H. Schwendener,⁴ D. Scislowski,²⁷ J. Secrest,^{14,33} M. Seddighin,³ L. Segui,¹⁸ S. Seibert,¹⁴ I. Semenec,^{3,4}
 F. Shaker,¹² T. Shantz,^{6,4} M. K. Sharma,³⁴ J. Shen,¹⁴ T. M. Shokair,¹⁴ L. Sibley,¹² J. Simms,¹⁸ J. R. Sinclair,¹³
 K. Singh,¹² P. Skensved,³ M. Smiley,^{8,9} T. Sonley,^{6,3} M. St-Amant,⁶ R. Stainforth,²¹ S. Stankiewicz,⁶ M. Strait,¹⁹
 M. I. Stringer,^{7,13} A. Stripay,^{6,3} R. Svoboda,¹⁰ S. Tacchino,^{3,6} R. Tafirout,²⁴ B. Tam,^{18,3} C. Tanguay,⁴
 J. Tatar,²⁷ L. Tian,³ N. Tolich,²⁷ J. Tseng,¹⁸ H. W. C. Tseung,²⁷ E. Turner,¹⁸ E. Vázquez-Jáuregui,^{23,6,4}
 S. Valder,¹³ R. Van Berg,¹⁴ J. G. C. Veinot,³⁵ C. J. Virtue,⁴ B. von Krosigk,¹⁷ J. M. G. Walker,²¹ M. Walker,³
 J. Wallig,⁹ S. C. Walton,⁴ F. Wang,^{31,32} J. Wang,¹⁸ M. Ward,³ J. Waterfield,¹³ J. J. Weigand,³⁶ R. F. White,¹³
 J. F. Wilkerson,²⁵ J. R. Wilson,^{20,7} J. D. Wilson,¹² T. J. Winchester,²⁷ P. Woosaree,⁴ A. Wright,³ S. Yang,¹²
 K. Yazigi,¹² Z. Ye,¹⁴ M. Yeh,¹¹ S. Yu,^{3,4} T. Zhang,¹⁰ Y. Zhang,^{31,32,12} T. Zhao,³ K. Zuber,^{17,37} and A. Zummo¹⁴

(The SNO+ Collaboration)

¹Laboratório de Instrumentação e Física Experimental de Partículas (LIP),
 Av. Prof. Gama Pinto, 2, 1649-003, Lisboa, Portugal

²Universidade de Lisboa, Instituto Superior Técnico (IST),
 Departamento de Física, Av. Rovisco Pais, 1049-001 Lisboa, Portugal

³Queen's University, Department of Physics, Engineering Physics & Astronomy, Kingston, ON K7L 3N6, Canada

⁴Laurentian University, School of Natural Sciences,
 935 Ramsey Lake Road, Sudbury, ON P3E 2C6, Canada

⁵Laboratório de Instrumentação e Física Experimental de Partículas (LIP), 3004-516, Coimbra, Portugal

⁶SNOLAB, Creighton Mine #9, 1039 Regional Road 24, Sudbury, ON P3Y 1N2, Canada

⁷Queen Mary, University of London, School of Physics and Astronomy, 327 Mile End Road, London, E1 4NS, UK

⁸University of California, Berkeley, Department of Physics, CA 94720, Berkeley, USA

⁹Lawrence Berkeley National Laboratory, 1 Cyclotron Road, Berkeley, CA 94720-8153, USA

¹⁰University of California, Davis, 1 Shields Avenue, Davis, CA 95616, USA

- ¹¹ Brookhaven National Laboratory, P.O. Box 5000, Upton, NY 11973-500, USA
- ¹² University of Alberta, Department of Physics, 4-181 CCIS, Edmonton, AB T6G 2E1, Canada
- ¹³ University of Sussex, Physics & Astronomy, Pevensey II, Falmer, Brighton, BN1 9QH, UK
- ¹⁴ University of Pennsylvania, Department of Physics & Astronomy,
209 South 33rd Street, Philadelphia, PA 19104-6396, USA
- ¹⁵ Laboratório de Instrumentação e Física Experimental de Partículas, Rua Larga, 3004-516 Coimbra, Portugal
- ¹⁶ Universidade de Coimbra, Departamento de Física (FCTUC), 3004-516, Coimbra, Portugal
- ¹⁷ Technische Universität Dresden, Institut für Kern und Teilchenphysik, Zellescher Weg 19, Dresden, 01069, Germany
- ¹⁸ University of Oxford, The Denys Wilkinson Building, Keble Road, Oxford, OX1 3RH, UK
- ¹⁹ The Enrico Fermi Institute and Department of Physics,
The University of Chicago, Chicago, IL 60637, USA
- ²⁰ King's College London, Department of Physics,
Strand Building, Strand, London, WC2R 2LS, UK
- ²¹ University of Liverpool, Department of Physics, Liverpool, L69 3BX, UK
- ²² Boston University, Department of Physics, 590 Commonwealth Avenue, Boston, MA 02215, USA
- ²³ Universidad Nacional Autónoma de México (UNAM),
Instituto de Física, Apartado Postal 20-364, México D.F., 01000, México
- ²⁴ TRIUMF, 4004 Westbrook Mall, Vancouver, BC V6T 2A3, Canada
- ²⁵ University of North Carolina, Department of Physics and Astronomy,
Phillips Hall, Chapel Hill, NC 27599-3255, USA
- ²⁶ Universidade de Lisboa, Faculdade de Ciências (FCUL),
Departamento de Física, Campo Grande, Edifício C8, 1749-016 Lisboa, Portugal
- ²⁷ University of Washington, Center for Experimental Nuclear Physics and Astrophysics,
and Department of Physics, Seattle, WA 98195, USA
- ²⁸ Idaho State University, 921 S. 8th Ave, Mail Stop 8106, Pocatello, ID 83209-8106
- ²⁹ Norwich University, 158 Harmon Drive, Northfield, VT 05663, USA
- ³⁰ Lancaster University, Physics Department, Lancaster, LA1 4YB, UK
- ³¹ Research Center for Particle Science and Technology,
Institute of Frontier and Interdisciplinary Science,
Shandong University, Qingdao 266237, Shandong, China
- ³² Key Laboratory of Particle Physics and Particle Irradiation of Ministry of Education,
Shandong University, Qingdao 266237, Shandong, China
- ³³ Armstrong Atlantic State University, 11935 Abercorn Street, Savannah, GA 31419, USA
- ³⁴ University of Alberta, Department of Chemistry, 1-001 CCIS, Edmonton, AB T6G 2E9, Canada
- ³⁵ University of Alberta, Department of Chemistry,
11227 Saskatchewan Drive, Edmonton, Alberta, T6G 2G2, Canada
- ³⁶ Technische Universität Dresden, Faculty of Chemistry and Food Chemistry, Dresden, 01062, Germany
- ³⁷ MTA Atomki, 4001 Debrecen, Hungary
- (Dated: May 8, 2025)

The SNO+ collaboration reports its second spectral analysis of reactor antineutrino oscillation using 286 tonne-years of new data. The measured energies of reactor antineutrino candidates were fitted to obtain the second-most precise determination of the neutrino mass-squared difference $\Delta m_{21}^2 = (7.96_{-0.42}^{+0.48}) \times 10^{-5} \text{ eV}^2$. Constraining Δm_{21}^2 and $\sin^2 \theta_{12}$ with measurements from long-baseline reactor antineutrino and solar neutrino experiments yields $\Delta m_{21}^2 = (7.58_{-0.17}^{+0.18}) \times 10^{-5} \text{ eV}^2$ and $\sin^2 \theta_{12} = 0.308 \pm 0.013$. This fit also yields a first measurement of the flux of geoneutrinos in the Western Hemisphere, with 73_{-43}^{+47} TNU at SNO+.

Introduction. Neutrino oscillation is well established through measurements of neutrino rates and energy spectra from particle accelerators, nuclear reactors, the atmosphere, and the Sun. These measurements provide consistent values for the three neutrino oscillation angles θ_{ij} and two mass-squared differences $\Delta m_{ij}^2 \equiv m_i^2 - m_j^2$, where i and j are 1, 2, or 3 ($i \neq j$). Leading measurements of Δm_{21}^2 , θ_{13} , and Δm_{32}^2 have been obtained with reactor antineutrinos [1–4]. The KamLAND experiment has made the most precise measurement of Δm_{21}^2 , along with a less sensitive measurement of $\sin^2 \theta_{12}$ [1]. In contrast, solar neutrino experiments have provided the most precise measurement of $\sin^2 \theta_{12}$ while being less sensi-

tive to Δm_{21}^2 . The KamLAND measurement of Δm_{21}^2 is currently in 1.5σ tension with the result of a combined analysis of all available solar neutrino data performed by Super-K [5].

SNO+ has previously published results studying reactor antineutrinos, including the first evidence of reactor antineutrino detection with a water Cherenkov detector [6] and an initial measurement of reactor antineutrino oscillation with the detector nearly half-filled with liquid scintillator [7]. Radioactive decays within the Earth also produce antineutrinos, which have been observed by the KamLAND and Borexino liquid scintillator detectors in Japan and Italy, respectively [8, 9]. This Letter presents

a measurement of Δm_{21}^2 and $\sin^2 \theta_{12}$ using reactor antineutrinos, and initial constraints on the geoneutrino flux, based on the first data collected by SNO+ as a fully-filled liquid scintillator detector.

Data. The SNO+ detector now contains about 780 tonnes of liquid scintillator within its 6.0-m radius spherical acrylic vessel (AV). Light produced by interactions in the scintillator is detected by 9362 inward-facing photomultiplier tubes (PMTs) at a radius of about 8.5 m. The scintillator volume is shielded by ultrapure water between the AV and PMTs and also beyond, where outward-looking PMTs are used to detect muons. The SNO+ detector is described in detail in Ref. [10].

The livetime of the dataset used in this analysis is 134.4 days, collected between May 17, 2022, and March 14, 2023. During this period, the scintillator was linear alkylbenzene (LAB) with 2,5-Diphenyloxazole (PPO) at a concentration of 2.2 g/L. The collected scintillation light yield was measured to be about 210 ‘clean’ PMT hits/MeV, which depends on the number of working channels and includes the removal of hits due to electronic noise and exclusion of channels that are not considered well calibrated in terms of charge and timing. The trigger threshold for this dataset was around 20 PMT hits, corresponding to approximately 0.09 MeV, well below the energy of the reactor antineutrino signals of interest.

The properties of particle interactions are inferred using the times and locations of hit PMTs. The time of flight of the photons detected by the PMTs is used to reconstruct the interaction position. The number of hit PMTs is approximately proportional to the energy deposited by a particle. The position-dependent efficiency to detect photons and the probability of detecting multiple photons on individual PMTs are accounted for in the energy reconstruction using Monte Carlo (MC) simulations. The resolution of the reconstructed energy E is about $6.5\%/\sqrt{E}$ for an electron at the center of the detector in this dataset. The reconstructed position resolution for a 2.5-MeV electron at the center is 12 cm in each of the three Cartesian axes.

Calibrations. Calibrations were performed using ^{214}Bi β decays and ^{214}Po α decays identified by their delayed coincidence. These decays were sourced by the ^{238}U intrinsic to the detector as well as ingress of ^{222}Rn into the scintillator. The selection criteria described in Table I, which include the time (Δt) and distance (Δr) between reconstructed interactions, provide a highly-pure sample of $^{214}\text{BiPo}$ coincidences.

The time profile of the scintillator is modeled for both α and β particles as a sum of exponentials with a single rise time parameter. The decay constants and amplitudes are tuned to provide the best match between the time-of-flight-corrected hit times in data and Monte Carlo (MC) simulation. This calibration is performed for β ’s and α ’s separately since α ’s produce a broader time profile.

The scintillator light yield and quenching are described with Birks’ law, which is tuned using the PMT hit spec-

TABLE I. Selection criteria applied to data and simulations to select $^{214}\text{BiPo}$ and Reactor- $\bar{\nu}$ IBD coincidence events. See text for parameter definitions.

	$^{214}\text{BiPo}$		Reactor- $\bar{\nu}$ IBD	
	Prompt	Delayed	Prompt	Delayed
E (MeV)	1.25-3.0	0.7-1.1	0.9-9.0	1.85-2.5
R (m)	0-4.0	0-4.0	0-5.7	0-5.7
Δr (m)	0-1.0		0-2.5	
Δt (μs)	3.7-1000		0-2000	
LR			>-3.5	

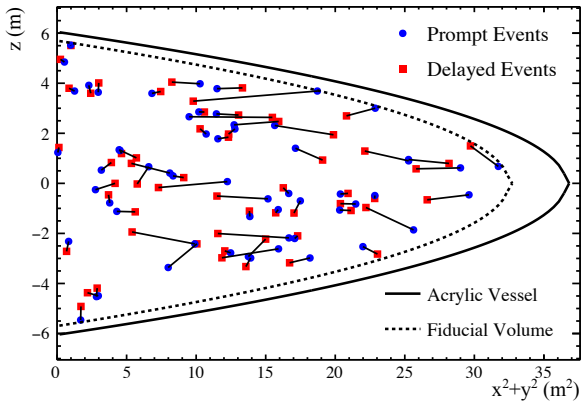
tra of the $^{214}\text{BiPo}$ coincidence events, following the procedure described in the previous analysis [7]. A single light yield is tuned by matching MC simulations of ^{214}Bi to data, while the Birks’ constant for β ’s, α ’s, and protons are each modeled with a distinct, tuned value. The newly-fit values are consistent with those of the previous analysis.

After these calibrations were performed, a residual nonuniformity of the energy scale was observed as a function of position nearer the AV. Empirical corrections for both data and simulation were created by fitting the mean energies of the selected $^{214}\text{BiPo}$ in bins of the vertical position z and the squared horizontal radius $\rho^2 \equiv (x^2 + y^2)$. A bilinear interpolation function was used to provide a continuous correction throughout the volume of the AV. After applying the correction, the uncertainties on the energy scale and resolution were evaluated as differences between the data and simulation to be 1.8% and $4.4\% \times \sqrt{E}$ (relative), respectively. These uncertainties were consistent between the β ’s and α ’s.

Antineutrino selection. Nuclear reactors produce a large, pure flux of $\bar{\nu}_e$ with energies up to around 10 MeV in the beta decays of nuclear fission products. These antineutrinos can be detected via the inverse beta decay (IBD) interaction on hydrogen atoms in the detector medium: $\bar{\nu}_e + p \rightarrow e^+ + n$. This process has a 1.8-MeV threshold and produces a positron, which quickly annihilates with an electron in the medium, depositing a total energy of $E_{\text{dep}} \approx E_{\bar{\nu}_e} - 0.8$ MeV in the detector. The neutron thermalizes and captures on hydrogen with a lifetime of about 200 μs , producing a 2.2-MeV γ . The coincidence of these prompt and delayed events provides a distinct signal to identify reactor antineutrinos, greatly reducing backgrounds.

Reactor antineutrino candidates are selected using the criteria summarized in Table I. A likelihood ratio (LR) is used to provide additional suppression of accidental coincidences. Similar to the LR method used in the analysis of the SNO+ water phase [6], the probability density functions (PDFs) for reactor- $\bar{\nu}$ IBDs come from MC simulations, and the PDFs for accidentals are constructed from a data sample of randomly-paired events that pass the prompt and delayed event criteria. The LR is then calculated from the products of the 2D PDF of Δt versus

FIG. 1. Positions of selected prompt and delayed events.



Δr and the 1D PDF of the delayed event E . In addition, Bayesian priors are applied to account for the rates of reactor- $\bar{\nu}$ IBDs and accidentals. A cut of -3.5 on the LR was determined by maximizing a ratio of signal (S) and background (B) counts: $S/\sqrt{S+B}$.

A suite of cuts designed to remove instrumental backgrounds is applied to all events. All data within the 20 seconds following an identified muon or high-energy event are removed to avoid cosmogenically-induced backgrounds. Additionally, any potential background from fast neutrons produced by muons in the external water is mitigated by removing events within 10 μ s of an event with 3 or more hit outward-looking PMTs. Event pairs that pass the $^{214}\text{BiPo}$ selection criteria in Table I or have additional coincident events, are also removed.

After applying all selection criteria, 59 coincidence pairs are observed in the dataset. The distributions of Δt , Δr , and delayed reconstructed energy of these coincidences are in good agreement with expectations for neutron captures, which were obtained by simulations of reactor- $\bar{\nu}$ IBDs [11]. Figure 1 shows the position distribution of the selected pairs, which are found to be uniform throughout the detector, as expected.

Reactor antineutrinos. Over 99% of the expected reactor antineutrino flux at SNO+ comes from reactors in North America, around 60% of which comes from Ontario's three Canadian Deuterium Uranium (CANDU) reactor complexes at baselines of 240 km, 340 km, and 350 km. Neutrino oscillations across these distances result in multiple dips in the detected prompt energy spectrum, which are well preserved given the large contribution of the CANDU reactors to the total flux.

The flux is modeled using the thermal power outputs of reactor cores as a function of time, the average fractions of the four dominant fissile isotopes, the average energy released per fission [12], and the emitted antineutrino energy spectra per isotope. Monthly-averaged thermal powers from yearly IAEA reports [13, 14] are used for all reactors except the CANDU reactors for which we use the hourly electrical output provided by IESO's

Generator Output and Capability reports [15]. These two reports show an average difference of $(+0.2 \pm 0.1)\%$ in reactor power over a period of a year. The fission fractions of ^{235}U , ^{238}U , ^{239}Pu and ^{241}Pu depend on reactor type and also vary over time, due to the depletion of isotopes and refueling cycles. Average values of (0.568, 0.078, 0.297, 0.057) [16] are used for the large number of pressurized water reactors (PWR) and boiling water reactors (BWR). The CANDU reactors use the pressurized heavy water reactor (PHWR) fission fractions (0.52, 0.05, 0.42, 0.01) [17], which are stabilized by continuous refueling and are averaged over multiple cores in each complex. Finally, the antineutrino energy spectrum emitted for each isotope is given by the Huber-Mueller model [18, 19]. The flux of the isotope model is known to be biased and is corrected by scaling by a factor of 0.945 ± 0.007 to match the global average of reactor flux measurements [20].

Several uncertainties on the flux are carried over from the detailed studies made by the Daya Bay experiment [20]. Per core, they include a 2.4% uncertainty from the isotopic emission spectra, 0.6% from fission fraction uncertainties, 0.5% from power output, and several other subdominant contributions. Studies carried out by the SNO+ collaboration produced consistent numbers. The uncertainties on the shape of the predicted energy spectrum [20] are expected to have a smaller impact than the detector-related uncertainties, and to be negligible.

The number of target protons available to produce IBDs is defined by the fiducial volume. An uncertainty on the size of the volume is determined from the position reconstruction and an uncertainty on the number of protons is inherited from the proton density in the liquid scintillator cocktail. The former is estimated to result in less than 1% uncertainty on the volume and the latter is computed from the scintillator mass density and the hydrogen mass fractions of all included compounds. The uncertainty on mass density from measurements and temperature variations was found to be less than 0.5%. Hydrogen mass fractions of the various carbon chains are very similar, and deviations many times larger than the manufacturer's limits would be required to produce even a modest impact on the proton density. However, Daya Bay assigned a 0.92% uncertainty to their proton number, primarily based on deviations of these mass fractions from combustion measurements [20]. In the absence of a direct independent measurement for the SNO+ cocktail, we conservatively adopt the same uncertainty.

The coincidence selection efficiency is obtained from MC simulations of IBDs occurring in the full scintillator volume, and is found to be 70%. Within the fiducial radius of 5.7 m, the efficiency is 83%. With subpercent biases resulting from position and energy reconstruction uncertainties, all aforementioned uncertainties total to produce a 3% uncertainty on the normalization of the reactor flux.

Neutrino oscillations. More than 95% of the incoming $\bar{\nu}_e$ flux is expected to travel entirely through the North American continental crust, which has a relatively con-

stant density [21, 22]. Therefore, the electron antineutrino survival probability is calculated using a full three-flavor mixing framework, accounting for the effect of constant matter density [23]:

$$P_{ee} = 1 - 4 \sum_{n>m} (X_n)_{ee} (X_m)_{ee} \sin^2 \left((\mathcal{E}_n - \mathcal{E}_m) \frac{L}{4E} \right),$$

where L and E are the baseline and antineutrino energy, respectively. All other quantities are defined in Ref. [23] and depend on θ_{12} , θ_{13} , Δm_{21}^2 , Δm_{31}^2 , E and the crust's electron density ($8.13 \times 10^{23} \text{ cm}^{-3}$). The matter effect induces a change in the flux of $\mathcal{O}(1\%)$ or less, and similarly, an $\mathcal{O}(1\%)$ change is induced in the effective $\widehat{\Delta m_{21}^2}$. For $\sin^2 \theta_{12} = 0.307$ and $\Delta m_{21}^2 = 7.53 \times 10^{-5} \text{ eV}^2$ [24], approximately 100 reactor- $\bar{\nu}$ IBD interactions are expected within the AV per year.

Geoneutrinos. Antineutrinos up to about 3.3 MeV are produced by β decays within the Earth. Only decays from the ^{238}U and ^{232}Th chains produce $\bar{\nu}_e$'s with energy greater than the IBD threshold. Methods based on Ref. [25] are used to predict the expected geoneutrino flux at SNO+ in Terrestrial Neutrino Units (TNU), where 1 TNU corresponds to 1 IBD interaction per year per 10^{32} free protons. Assuming a constant survival probability of $\langle P_{ee} \rangle = 0.55$ and a radiogenic heat of 20 TW, our model predicts geo- $\bar{\nu}$ IBD rates of 36.3 ± 8.7 TNU and 9.7 ± 2.3 TNU from the ^{238}U and ^{232}Th chains, respectively. This gives an expected rate of 27 geo- $\bar{\nu}$ IBDs within the AV per year. Recognizing uncertainty in the range of possible Earth radiogenic heat values and in the local geology, the total geo- $\bar{\nu}$ IBD rate is fit without a direct constraint. As in geoneutrino studies by KamLAND and Borexino, knowledge of Earth's Th and U chondritic abundances [26] motivates applying a constraint on the ratio of U/Th geo- $\bar{\nu}$ IBD event rates when fitting the data. In this analysis, we use the predicted fluxes from our model to derive a constraint on the U/Th ratio of 3.7 ± 1.3 , where the uncertainty comes from combining each of the U and Th flux prediction uncertainties.

(α, n) backgrounds. The dominant background in this analysis is from (α, n) interactions with the natural ^{13}C present in the scintillator. These interactions produce ^{16}O and a neutron, which thermalizes and captures, mimicking the IBD delayed signal. The prompt event can proceed through three channels, each producing a distinct energy peak. The neutron can elastically scatter protons, producing a signal in the apparent energy range of roughly 0.5 MeV to 3.5 MeV, or it can inelastically scatter off a ^{12}C , which emits a 4.4-MeV γ . Alternatively, the ^{16}O can be produced in an excited state, de-exciting by producing either a 6-MeV γ or an electron-positron pair that deposits about 6 MeV.

The dominant source of α decays in the detector is ^{210}Po . The rate of these decays is measured over time with a fit of the α 's energy peak, which quenches to be around 0.4 MeV. The (α, n) background from ^{210}Po implanted on the surface of the AV is reduced to a negligible

level by the fiducial volume selection. The average rate within the fiducial volume over this dataset is 38 Hz, nearly a factor of 5 reduction in specific ^{210}Po activity compared to the initial oscillation measurement, as described in Ref. [7].

The probability of the ^{210}Po α undergoing an (α, n) interaction is calculated by integrating the energy-dependent interaction cross section up to the ^{210}Po α energy, and then multiplying by the ^{13}C number density, in the same way as Ref. [7]. This, combined with the average ^{210}Po rate, gives an average expected (α, n) rate of 0.21 events/day.

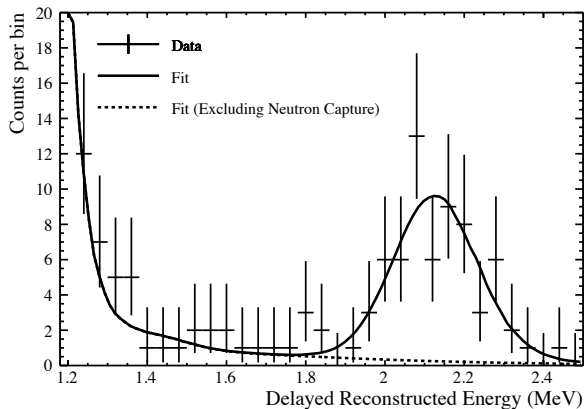
Disagreements between total cross section measurements and particularly large uncertainties in branching ratios (ground state vs. excited state) warrant a conservative approach to (α, n) uncertainties [27]. The uncertainties from Ref. [7] are assigned to the normalizations of the three (α, n) interaction channels: for proton elastic scatters and the ^{12}C inelastic scatter, 30% uncertainties are assigned, and for the excited ^{16}O channel, a 100% uncertainty is assigned.

$^{214}\text{BiPo}$ -like background. Immediately after scintillator filling operations, the data showed higher rates of radioactive backgrounds primarily due to ingress of radon, resulting in most of these backgrounds decaying away with the ^{222}Rn half-life of 3.8 days. During these high-background periods, an excess of coincidences was observed with delayed event energies just below the 2.2-MeV region of interest. The Δt and Δr distributions of these coincidences were consistent with a correlated decay of time and distance similar to those of IBD and $^{214}\text{BiPo}$ coincident events, and the position distribution was uniform.

The prompt energy distribution of these events is in good agreement with the ^{214}Bi β decay spectrum ($Q = 3.3$ MeV) that precedes a ^{214}Po α decay, which has an energy of 7.8 MeV, but quenches down to about 0.8 MeV in visible energy in the scintillator. The half-life of the ^{214}Po decay is 164 μs , which is close to the approximately 210- μs neutron capture time for IBDs. Rare $\alpha + \gamma$ decays of ^{214}Po are too low in energy to create the excess. A likely explanation is that these tails arise from alpha-proton elastic scattering interactions, in which more scintillation light is produced than by the α 's alone due to the lesser quenching of protons. Data show that α decays of ^{215}Po exhibit a similar tail extending to higher energies.

For this analysis, a data-driven model of the ^{214}Po energy spectrum was created using a kernel density estimation of the ^{215}Po energy distribution. Figure 2 shows that the model fits well to the delayed energy spectrum, which is dominated by ^{214}Po in the lower half. The corresponding prompt energy is modeled as ^{214}Bi . The LR can help suppress this type of background due to the differences in the delayed energy distributions between ^{214}Po and 2.2-MeV neutron capture γ 's. Across the dataset used in the present analysis, the model predicts that 1.1 ± 1.1 $^{214}\text{BiPo}$ coincidence events will pass the IBD selection

FIG. 2. Fit of extended delayed energy distribution. The model includes a data-driven kernel density estimate of the ^{214}Po spectrum based on the observed spectrum of ^{215}Po . ^{214}Po backgrounds, which dominate the lower half of the spectrum, were increased in this plot relative to the analyzed data via the inclusion of data from the period immediately after scintillator fill operations, when radon levels in the detector were elevated.



criteria, which has a small effect on sensitivity estimates for Δm_{21}^2 [28].

Other backgrounds. The rate of accidental coincidences is calculated using the measured rates of events passing the selection criteria for prompt and delayed event candidates. After applying all selection criteria, including the LR cut, the calculation gives an expectation of 0.3 coincidences in the entire 134.4-day dataset. Since it is based directly on data, the prediction has a negligible uncertainty.

Atmospheric neutrinos can undergo neutral- and charged-current interactions with the hydrogen and carbon present in the scintillator, which can produce neutrons and mimic the IBD signal. A study of simulated atmospheric neutrino interactions at SNO+ was performed using the GENIE Monte Carlo generator [29] and found a negligible contribution relative to the expected IBD signal.

Cosmogenic muon interactions in the detector can produce neutrons and sources of $(\beta - n)$ decays. These backgrounds are reduced to a negligible level by the muon veto cuts.

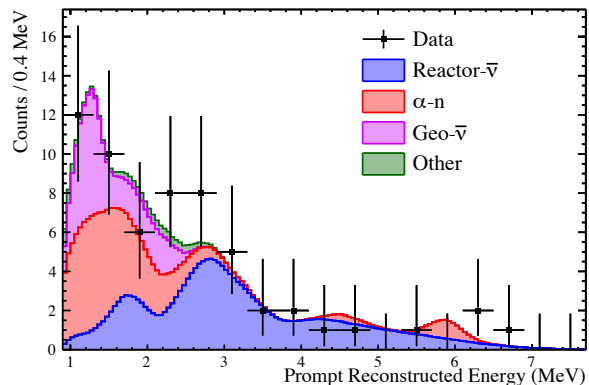
Spectral Analysis and Results. The expected numbers of signal and background events are listed in Table II and the corresponding prompt energy spectra are shown in Fig. 3. The total expected number of selected coincidences is 54.7, in reasonable agreement with the 59 coincidences observed in the data. Two independent analyses were performed to cross-check this event selection and the following fits.

A binned extended log likelihood fit was applied to the prompt energy distribution to find the best-fit values of Δm_{21}^2 and $\sin^2 \theta_{12}$. The data and fitted energy spectra are shown in Fig. 3. Nuisance parameters were

TABLE II. Expected and fitted numbers of signal and background events, and the total number of observed events in 134.4 days of data. Expectations show only systematic uncertainties and the geo- $\bar{\nu}$ IBD rate is unconstrained. The fits are with unconstrained or constrained oscillation parameters.

	Expectation	Fit (Uncon.)	Fit (Con.)
Reactor- $\bar{\nu}$ IBD	27.9 ± 0.8	$25.1^{+6.4}_{-2.1}$	27.5 ± 0.9
(α, n)	18.2 ± 5.2	$17.2^{+4.5}_{-4.4}$	$17.2^{+4.5}_{-4.4}$
Geo- $\bar{\nu}$ IBD	7.2	$12.0^{+7.4}_{-6.8}$	$11.1^{+7.1}_{-6.6}$
$^{214}\text{BiPo}$ -like	1.1 ± 1.1	1.2 ± 1.1	1.2 ± 1.1
Accidental	0.3 ± 0.0	0.3 ± 0.0	0.3 ± 0.0
Total	54.7	55.8	57.3
Observed	59	59	59

FIG. 3. Energy distribution of prompt events and best-fit (unconstrained) predictions.

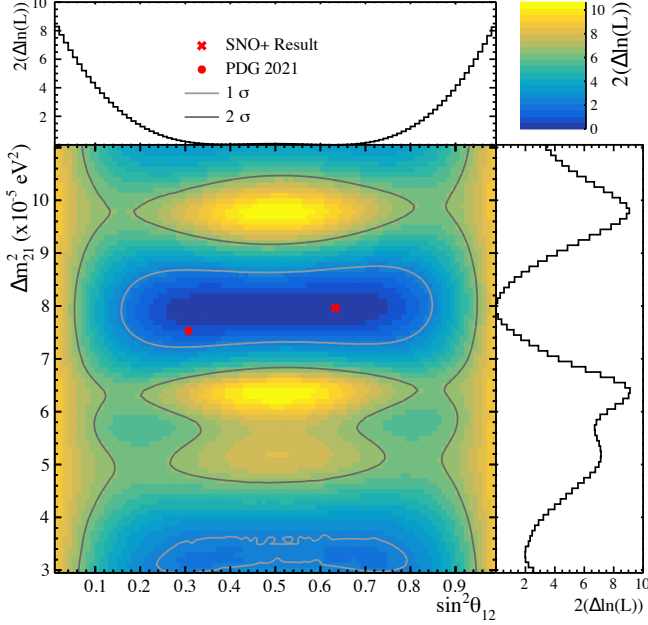


constrained with Gaussian penalty terms added to the likelihood function. These parameters include the normalizations on reactor- $\bar{\nu}$ IBDs, (α, n) channels, and the geoneutrino U/Th ratio, as well as energy systematics.

The uncertainties on the prompt energy are dominated by reconstruction uncertainties. The energy systematics are modeled as uncertainties in the energy scale – both linear and non-linear – and in the energy resolution. Two independent factors parameterize the linear energy scale uncertainties of β 's/ γ 's (1.8%) and protons (3%) to account for their different scintillation response. A non-linear scaling following Birks' law is applied as a variation in Birks' constant k_B (5.4%). Finally, energy resolution uncertainty is modeled as a Gaussian smearing with a standard deviation of $4.4\% \times \sqrt{E}$ [27, 28].

A 2D visualization of the measurement significance is shown in Fig. 4 as a grid scan of the log likelihood over Δm_{21}^2 and $\sin^2 \theta_{12}$, profiling over all other parameters. Performing a complete fit to account for correlations between all parameters, the best-fit values for the unconstrained oscillation parameters are $\Delta m_{21}^2 = (7.96^{+0.48}_{-0.42}) \times 10^{-5} \text{ eV}^2$ and $\sin^2 \theta_{12} = 0.62^{+0.16}_{-0.40}$. A nearly equally significant result for $\sin^2 \theta_{12}$ occurs at the mirror

FIG. 4. The log likelihood of the prompt energy spectrum as a function of Δm_{21}^2 vs. $\sin^2 \theta_{12}$ with 1σ and 2σ contours drawn. The log likelihood is also shown separately for each variable, fixing the other to the best-fit value. The slight asymmetry about 0.5 is expected and gives a second best-fit point for $\sin^2 \theta_{12}$ near the global result 0.307 [24].



value across 0.5. Combining the previous measurement from SNO+ [7] with the present result produces minimal change; therefore, it has not been included. The result for Δm_{21}^2 agrees with the KamLAND result, $(7.53 \pm 0.18) \times 10^{-5} \text{ eV}^2$ [1], within 1σ . It shows a slightly worse agreement of 1.3σ with the combined solar result from Super-K, $(6.10^{+0.95}_{-0.81}) \times 10^{-5} \text{ eV}^2$ [5].

The fit is repeated assuming Gaussian constraints of $\Delta m_{21}^2 = (7.53 \pm 0.18) \times 10^{-5} \text{ eV}^2$ [1] and $\sin^2 \theta_{12} = 0.307 \pm 0.013$ [30]. The fitted number of geo- $\bar{\nu}$ IBDs is $11.1^{+7.1}_{-6.6}$, which corresponds to a geo- $\bar{\nu}$ IBD rate of 73^{+47}_{-43} TNU. The measured geoneutrino rate has a relatively large uncertainty, making it consistent with the range of existing Earth models allowed by the two previous measurements. The uncertainty in the geo- $\bar{\nu}$ IBD rate is dominated by a negative correlation with the proton scattering component of (α, n) and is not significantly improved by constraining the oscillation parameters. The resulting best-fit oscillation parameters are $\Delta m_{21}^2 = 7.58^{+0.18}_{-0.17} \times 10^{-5} \text{ eV}^2$ and $\sin^2 \theta_{12} = 0.308 \pm 0.013$. The tension between solar and reactor results for Δm_{21}^2 , after combining SNO+ and KamLAND, is slightly greater than 1.5σ . Table III summarizes the results of the two different fits. All nuisance parameters are found to be in good agreement with expectations in both cases. Given that $\sin^2 \theta_{12}$ is largely determined by the flux and Δm_{21}^2 by the spectrum, the two parameters are minimally correlated, leaving little to gain by constraining one and fitting the other.

TABLE III. Best-fit values for oscillation parameters and geo- $\bar{\nu}$ IBD rate. Results are reported with no constraints on oscillation parameters Δm_{21}^2 and $\sin^2 \theta_{12}$, and with Gaussian constraints according to their current best measurements (see text).

	Fit (Uncon.)	Fit (Con.)
$\Delta m_{21}^2 (\times 10^{-5} \text{ eV}^2)$	$7.96^{+0.48}_{-0.42}$	$7.58^{+0.18}_{-0.17}$
$\sin^2 \theta_{12}$	$0.62^{+0.16}_{-0.40}$	0.308 ± 0.013
Geo- $\bar{\nu}$ IBD rate (TNU)	79^{+49}_{-44}	73^{+47}_{-43}

Future sensitivities. The sensitivity of this measurement is still limited by statistics and SNO+ is continuing to take data. The detector has been loaded with a secondary fluor (bis-MSB), increasing the light collected by more than 50%, and loading of tellurium is scheduled to begin in 2025. New data have been obtained with the enhanced light collection and sensitivity will remain similar when filled with tellurium, allowing continued study of reactor antineutrino oscillations and geoneutrinos.

Development of a novel event classifier showing improved rejection of the (α, n) background, as discussed in Ref. [7], is ongoing. Because the (α, n) proton scatter events have an energy range similar to geo- $\bar{\nu}$ IBDs, reduction of the (α, n) background is predicted to significantly improve the sensitivity to the geo- $\bar{\nu}$ IBD rate.

Summary. The SNO+ collaboration reports the second-most precise measurement of Δm_{21}^2 , using reactor antineutrinos. We find $\Delta m_{21}^2 = (7.96^{+0.48}_{-0.42}) \times 10^{-5} \text{ eV}^2$ while also measuring $\sin^2 \theta_{12} = 0.62^{+0.16}_{-0.40}$. When applying Gaussian constraints according to external values of Δm_{21}^2 and $\sin^2 \theta_{12}$, we obtain a measurement of $\Delta m_{21}^2 = 7.58^{+0.18}_{-0.17}$ and of the geo- $\bar{\nu}$ IBD rate: 73^{+47}_{-43} TNU.

ACKNOWLEDGMENTS

Capital funds for SNO+ were provided by the Canada Foundation for Innovation and matching partners: Ontario Ministry of Research, Innovation and Science, Alberta Science and Research Investments Program, Queen's University at Kingston, and the Federal Economic Development Agency for Northern Ontario. This research was supported by *Canada*: the Natural Sciences and Engineering Research Council of Canada, the Canadian Institute for Advanced Research, the Ontario Early Researcher Awards, the Arthur B. McDonald Canadian Astroparticle Physics Research Institute; *U.S.*: the Department of Energy (DOE) Office of Nuclear Physics, the National Science Foundation and the DOE National Nuclear Security Administration through the Nuclear Science and Security Consortium; *UK*: the Science and Technology Facilities Council and the Royal Society; *Portugal*: Fundação para a Ciência e a Tecnologia (FCT-Portugal); *Germany*: the Deutsche Forschungsgemeinschaft; *Mexico*: DGAPA-UNAM and Consejo

Nacional de Ciencia y Tecnología; *China*: the Discipline Construction Fund of Shandong University. We also thank SNOLAB and SNO+ technical staff; the Digital Research Alliance of Canada; the GridPP Collaboration and support from Rutherford Appleton Laboratory; and the Savio computational cluster at the University of California, Berkeley. Additional long-term storage was

provided by the Fermilab Scientific Computing Division.

For the purposes of open access, the authors have applied a Creative Commons Attribution licence to any Author Accepted Manuscript version arising. Representations of the data relevant to the conclusions drawn here are provided within this paper and its supplemental material.

-
- [1] A. Gando et al. (KamLAND), Phys. Rev. D **88**, 033001 (2013), 1303.4667.
 - [2] F. P. An et al. (Daya Bay), Phys. Rev. Lett. **130**, 161802 (2023), 2211.14988.
 - [3] G. Bak et al. (RENO), Phys. Rev. Lett. **121**, 201801 (2018), 1806.00248.
 - [4] H. de Kerret et al. (Double Chooz), Nature Phys. **16**, 558 (2020), 1901.09445.
 - [5] K. Abe et al. (Super-Kamiokande), Phys. Rev. D **109**, 092001 (2024), 2312.12907.
 - [6] A. Allega et al. (SNO+), Phys. Rev. Lett. **130**, 091801 (2023), 2210.14154.
 - [7] A. Allega et al. (SNO+), Eur. Phys. J. C **85**, 17 (2025), 2405.19700.
 - [8] S. Abe et al. (KamLAND), Geophys. Res. Lett. **49** (2022), 2205.14934.
 - [9] M. Agostini et al. (Borexino), Phys. Rev. D **101**, 012009 (2020), 1909.02257.
 - [10] V. Albanese et al. (SNO+), JINST **16**, P08059 (2021), 2104.11687.
 - [11] See supplemental information.
 - [12] X. B. Ma, W. L. Zhong, L. Z. Wang, Y. X. Chen, and J. Cao, Phys. Rev. C **88**, 014605 (2013), 1212.6625.
 - [13] Operating Experience with Nuclear Power Stations in Member States (International Atomic Energy Agency, Vienna, 2022), URL <https://www.iaea.org/publications/15212/>.
 - [14] Operating Experience with Nuclear Power Stations in Member States (International Atomic Energy Agency, Vienna, 2023), URL <https://www.iaea.org/publications/15484/>.
 - [15] *Generator Output and Capability reports*, Generator Output and Capability (The Independent Electricity System Operator, Toronto, Ontario, Canada, 2023), URL <https://www.ieso.ca/Power-Data/Data-Directory>.
 - [16] K. Eguchi et al. (KamLAND), Phys. Rev. Lett. **90**, 021802 (2003), hep-ex/0212021.
 - [17] Atomic Energy of Canada Limited (AECL), Private communication (2013), <https://www.aecl.ca/>.
 - [18] P. Huber, Phys. Rev. C **84**, 024617 (2011), [Erratum: Phys.Rev.C 85, 029901 (2012)], 1106.0687.
 - [19] T. A. Mueller et al., Phys. Rev. C **83**, 054615 (2011), 1101.2663.
 - [20] D. Adey et al. (Daya Bay), Phys. Rev. D **100**, 052004 (2019), 1808.10836.
 - [21] G. S. Chulick and W. D. Mooney, Bulletin of the Seismological Society of America **92**, 2478 (2002).
 - [22] NOAA, *National centers for environmental information* (<https://www.ngdc.noaa.gov/>) (2012), URL <https://www.ngdc.noaa.gov/>.
 - [23] J. Page, Computer Physics Communications **300**, 109200 (2024), ISSN 0010-4655, URL <https://www.sciencedirect.com/science/article/pii/S0010465524001231>.
 - [24] P. A. Zyla et al. (Particle Data Group), PTEP **2020**, 083C01 (2020), and 2021 update.
 - [25] S. A. Wipperfurth, O. Šrámek, and W. F. McDonough, Geophys. Res. Solid Earth **125** (2019), 1907.12184.
 - [26] S. A. Wipperfurth, M. Guo, O. Šrámek, and W. F. McDonough, Earth Planet. Sci. Lett. **498** (2018).
 - [27] J. E. Page, Ph.D. thesis, University of Sussex (2025), URL https://sussex.figshare.com/articles/thesis/Reactor_antineutrino_oscillation_detection_in_liquid_scintillator_at_SNO_/28239767.
 - [28] A. Zummo, Ph.D. thesis, University of Pennsylvania, UPenn, Philadelphia (2024).
 - [29] C. Andreopoulos, A. Bell, D. Bhattacharya, F. Cavanna, J. Dobson, S. Dytman, H. Gallagher, P. Guzowski, R. Hatcher, P. Kehayias, et al., Nuclear Instruments and Methods in Physics Research Section A: Accelerators, Spectrometers, Detectors and Associated Equipment **614**, 87 (2010).
 - [30] K. Abe et al. (Super-Kamiokande), Phys. Rev. D **94**, 052010 (2016), 1606.07538.

SNO+ Experiment
Supplemental Material
May 2025

This document provides supplemental information relevant to the measurement of reactor antineutrinos oscillation in “Measurement of reactor antineutrino oscillation at SNO+”.

TABLE I. Information about the 59 coincidence pairs selected.

Prompt			Delayed			Δt (μ s)	Δr (cm)	Date
E (MeV)	$\sqrt{x^2 + y^2}$ (m)	z (m)	E (MeV)	$\sqrt{x^2 + y^2}$ (m)	z (m)			
1.81	4.18	-0.70	1.93	4.13	-1.19	73.92	56.30	20/05/2022
3.23	3.71	-2.92	2.09	3.87	-2.23	59.34	71.60	23/05/2022
1.16	3.96	2.31	2.13	4.46	1.94	330.78	62.42	26/05/2022
1.66	1.30	-5.46	2.30	1.31	-4.92	294.16	65.10	26/05/2022
2.58	1.78	0.53	2.17	1.98	0.83	132.10	35.95	27/05/2022
1.89	1.72	-4.49	2.11	1.48	-4.37	23.72	27.47	27/05/2022
1.50	5.03	0.90	1.98	4.70	1.29	133.82	51.06	27/05/2022
6.38	5.63	0.68	2.06	5.45	1.50	235.42	108.53	29/05/2022
1.02	3.40	1.78	2.28	3.51	1.84	83.44	19.45	30/05/2022
1.77	2.07	-1.12	2.03	2.37	-1.14	300.56	33.82	03/06/2022
2.29	4.08	-0.40	2.11	4.03	-0.18	15.88	25.45	08/06/2022
1.03	0.24	1.23	2.21	0.36	1.43	39.02	24.28	08/06/2022
2.68	3.38	2.78	2.18	3.61	2.73	74.48	30.80	13/06/2022
6.89	3.89	-0.62	2.09	3.39	-0.51	187.18	51.65	19/06/2022
1.14	4.63	-0.83	2.22	4.51	-0.81	45.30	13.27	20/06/2022
1.92	4.51	-0.43	2.04	4.57	-0.40	479.34	7.49	21/06/2022
0.96	2.57	0.66	2.24	2.40	-0.03	347.60	77.45	28/06/2022
1.88	5.44	-0.46	2.07	5.16	-0.66	13.62	37.13	30/06/2022
2.35	3.08	2.66	2.05	3.93	2.63	9.72	85.45	02/07/2022
2.28	4.78	3.00	2.13	4.56	2.70	86.30	48.38	02/07/2022
5.58	2.11	1.34	2.27	2.39	1.02	18.48	43.41	03/07/2022
3.14	5.06	-1.86	2.27	4.71	-0.97	579.92	96.01	30/07/2022
2.22	3.72	-1.33	1.95	3.72	-1.11	429.20	23.44	22/08/2022
4.59	2.83	-3.36	2.13	3.17	-2.42	181.10	102.55	01/09/2022
1.06	3.50	0.07	2.27	2.70	-0.17	90.56	83.50	02/09/2022
2.94	2.89	0.30	2.01	3.02	0.23	143.30	14.93	13/09/2022
6.12	3.53	-2.78	2.07	3.47	-2.70	267.00	29.87	16/09/2022
4.45	3.58	2.17	2.09	3.51	1.97	530.58	27.28	17/10/2022
1.45	3.27	1.97	2.07	3.21	2.18	212.66	35.09	27/10/2022
1.19	5.39	0.62	2.20	5.08	0.58	464.34	37.56	03/11/2022
2.90	1.51	3.92	2.07	1.56	3.60	182.32	34.52	04/11/2022
1.11	1.95	-0.78	2.25	1.92	-0.46	411.46	34.01	05/11/2022
0.95	4.33	3.69	2.17	3.13	3.28	279.48	138.17	08/11/2022
1.27	4.14	1.40	1.98	4.37	0.93	23.20	61.39	09/11/2022
1.56	0.73	4.85	2.05	0.49	4.95	300.60	30.62	11/11/2022
1.39	1.66	-0.25	2.19	2.04	-0.00	31.90	47.12	26/11/2022
2.90	4.78	-0.49	2.14	4.78	-0.60	13.74	12.53	27/11/2022
2.04	3.19	2.85	1.96	3.25	2.85	210.38	29.45	08/12/2022
2.42	3.15	-2.42	2.29	2.32	-1.94	156.88	104.04	10/12/2022
1.66	4.69	-2.53	2.35	4.80	-2.83	952.90	33.14	11/12/2022
1.25	1.12	3.69	2.13	0.93	3.80	82.82	26.61	24/12/2022
2.14	0.91	-2.32	2.02	0.83	-2.72	284.56	61.05	25/12/2022
2.84	3.39	3.78	2.33	3.65	3.81	511.54	40.21	29/12/2022
2.88	3.57	2.34	2.20	3.99	2.47	84.76	49.63	04/01/2023
3.47	3.99	-2.62	2.15	3.44	-2.97	7.00	65.82	04/01/2023
3.98	0.99	5.52	2.27	1.00	5.51	9.96	19.04	08/01/2023
2.10	1.72	3.64	2.08	1.73	4.01	5.44	53.56	09/01/2023
2.86	4.13	-2.20	2.20	4.16	-2.10	137.68	13.29	22/01/2023
3.58	5.03	0.95	2.17	5.31	0.80	5.42	32.20	27/01/2023
4.01	4.26	-2.98	2.16	4.09	-3.17	22.44	45.28	27/01/2023
1.61	4.51	-1.07	2.22	4.60	-1.08	371.46	13.48	28/01/2023
1.58	3.21	3.98	1.99	2.87	4.04	36.40	39.56	29/01/2023
1.40	4.08	-2.18	2.44	3.40	-2.00	52.44	72.07	03/02/2023
1.01	1.68	-4.53	2.09	1.70	-4.19	199.10	36.07	05/02/2023
2.91	2.13	1.31	2.01	2.15	1.19	229.16	12.36	11/02/2023
2.22	3.73	-2.98	2.03	3.68	-3.33	445.90	36.39	14/02/2023
2.93	2.85	0.41	2.10	2.31	0.80	212.56	77.33	16/02/2023
2.84	3.99	-1.05	2.15	3.96	-1.18	58.36	13.12	25/02/2023
1.68	2.61	3.59	2.10	2.73	3.67	341.78	14.24	25/02/2023

EVENT DISTRIBUTIONS

FIG. 1. Time between prompt and delayed events (Δt) for both data and reactor IBD simulation. The exponential fit (red) results in a neutron capture time constant of $(197 \pm 32) \mu\text{s}$.

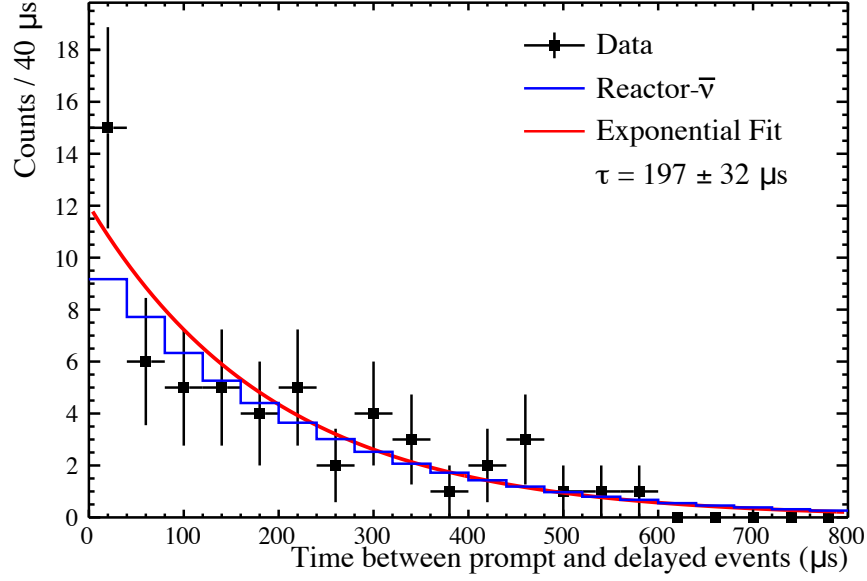


FIG. 2. Distance between prompt and delayed events (Δr) for both data and reactor IBD simulation.

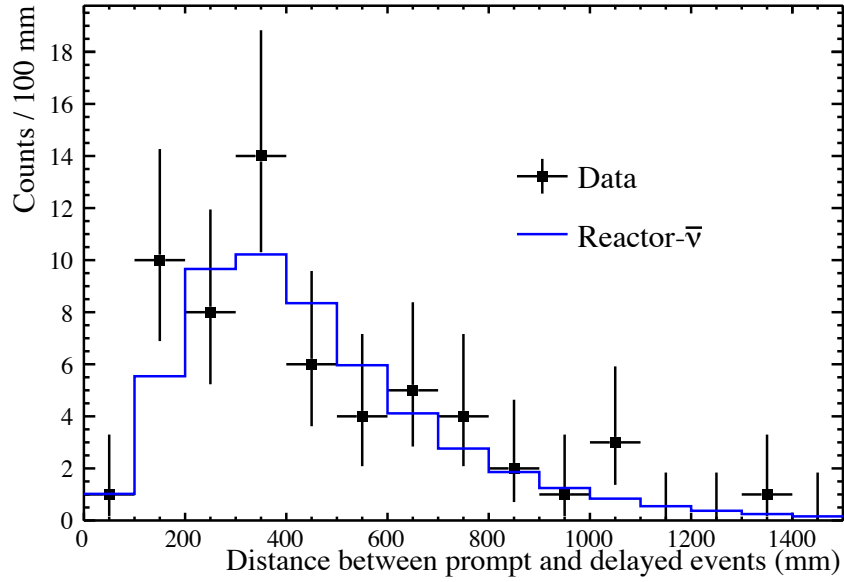


FIG. 3. Delayed event energy (E) for both data and reactor IBD simulation.

